Oxygen activation-boosted manganese oxide with unique interface for chlorobenzene oxidation: Unveiling the roles and dynamic variation of active oxygen species in heterogeneous catalytic oxidation process

Xiaoxiao Duan, Ting Zhao, Zhenwen Yang, Ben Niu, Ganggang Li, Bingzhi Li, Zhongshen Zhang [*], Jie Cheng [*], Zhengping Hao [*]

National Engineering Laboratory for VOCs pollution Control Material & Technology, Research Center for Environmental Material and Pollution Control Technology, University of Chinese Academy of Sciences, Beijing 101408, PR China

ARTICLE INFO

ABSTRACT

In-depth study of active oxygen species (AOS) is essential to heterogeneous catalytic oxidation techniques. Herein, a facile strategy of constructing dual-phase MnO_x with unique Mn_2O_3—Mn_3O_4 interface is reported for chlorobenzene (CB) catalytic oxidation. The interface induces lattice distortion and generates oxygen vacancies, promoting the formation and mobility of surface adsorbed oxygen (O_{ads}) and surface lattice oxygen (O_{latt}), while the surface acidity and CB adsorption capacity are also enhanced. Thereby, MnO_x catalyst exhibits superior activity and lower activation energy (41.7 kJ/mol), with the CB total degradation temperature decreasing by ca. 40 °C. Noteworthily, the dynamic variation of AOS in CB oxidation is unveiled by in situ techniques combined with isotope labelling, where O_{ads} and O_{latt} are determined to function as AOS at low and high temperatures (over 300 °C), respectively. Furthermore, the reaction pathway and the rate-determining step (cleavage of aromatic ring) are revealed by systematic mechanism study.

1. Introduction

Generating active oxygen species (AOS) is of great significance in heterogeneous catalytic oxidation reactions, where surface adsorbed oxygen (O_{ads}) and surface lattice oxygen (O_{latt}) are two predominant AOS in numerous catalytic oxidation processes. O_{ads} (O_2^-, O_2^{2-} and O^-) originate from the activation of chemisorbed O_2 molecules at active sites of catalysts (metal sites, oxygen vacancy, etc.) [1,2], while O_{latt} (O^{2-}) extensively exist on metal oxides. Boosting the generation and activation of oxygen species is crucial for activity promotion, which has been a challenging issue that needs continuous study. Catalytic oxidation of chlorinated volatile organic compounds (CVOCs) is a promising technique for CVOCs elimination, thus the research on AOS is also essential to environmental improvement. For reducible transition metal oxides, a class of versatile materials widely used in heterogeneous catalysis, constructing favorable adsorption and activation sites toward gaseous O_2 is advisable for facilitating O_{ads} formation, while enhancing the mobility of intrinsic oxygen species is a feasible strategy for improving the reactivity of O_{latt}. Until now, how to construct active sites and

mobilize oxygen species with easily-handled methods still needs in-depth study, which is critical for developing high-efficiency heterogeneous catalysts.

Tuning the natural structure of catalysts is effective in regulating diversified physicochemical features, including that of oxygen species. Recently, the construction of mixed-phase structure has been reported capable of ameliorating catalytic properties. Coupling two single-phase structures with different functions could integrate advantages and bring about superior activity [3]. More importantly, the existence of distinct phases would generate abundant interface structure, which is prone to induce lattice distortion and structural defects or alter electronic properties [4,5]. For instance, the formation of bimetallic interface triggered lattice contraction, weakening the adsorption of reaction intermediates and enhancing catalytic efficiency [6]. Metal—oxide interface was also unraveled to boost oxygen vacancy formation and O_2 activation, which in turn promoted catalytic performances [7–10]. Therefore, fabricating mixed-phases structure can be expected to diminish the formation and activation barrier of AOS, and this strategy could be applicable for optimizing manganese-based oxides (Mn_xO_y), which are a kind of

momentous catalysts in multifarious catalytic oxidation reactions [11]. Nevertheless, the regulation of Mn_xO_y catalysts involving constructing mixed phases has been rarely reported for now.

Although promoting the generation of active O_{ads}/O_{latt} is universally accepted crucial for catalytic oxidation, it is controversial whether O_{ads} or O_{latt} function as AOS in multifold oxidation reactions [12–16]. Fu et al. [1] reported dioxygen molecules were activated into reactive O_{ads} at coordinatively unsaturated Fe sites to react with CO, and Dai's group [17] revealed the hydrocarbon intermediates from C—Cl breakage were oxidized into CO_2 by O_{ads}. Differently, Nie et al. [14] proved that steam treatment activated O_{latt} on Pt/CeO_2, consequently promoting the low-temperature CO oxidation. He and co-workers [18] proposed O_{latt} facilitated electron transfer and enhanced the redox reaction of 1, 2-dichloroethane. Besides this divergence, it could be more important that dynamic variation of AOS emerges during reaction processes, which is dominantly associated with operation conditions (e.g. reaction temperature) [19,20]. Concretely, O_{ads} and O_{latt} were found to participate in toluene oxidation severally at low and high temperature [20]. Given the significance and complexity of AOS in catalytic oxidation, exploring the roles of O_{ads} and O_{latt} will be meaningful for promoting the activities of oxidation reactions.

Herein, we have fabricated dual-phase Mn_xO_y catalyst with interfacial structure via a simple solvothermal method, which is employed for catalytic oxidation of volatile organic compounds (VOCs) containing chlorine heteroatom (a typical harmful environmental pollutant). The abundant Mn_2O_3—Mn_3O_4 interface induces lattice mismatch/distortion and boosts the formation and mobility of O_{ads} and O_{latt}, consequently promoting the catalytic activity toward chlorobenzene (CB) deep oxidation and intermediates decomposition. What's more, the identification and variation of AOS in CB oxidation are explored by well-designed in situ TPD (temperature-programmed desorption) techniques, where O_{ads} and O_{latt} function as AOS at different temperature regions. Simultaneously, the reaction mechanism is revealed by in situ DRIFTS, and the cleavage of aromatic ring is determined as the rate-controlling step in CB oxidation. This work could not only extend the understanding of dynamic variation of AOS, but also provide an advisable strategy for developing high-activity catalysts for heterogeneous catalytic oxidation reactions including CVOCs oxidation.

2. Experimental

2.1. Catalyst preparation

Mn_2O_3 was synthesized via a solvothermal method. Specifically, quantitative manganese nitrate was dissolved in 60 mL isopropanol followed by the addition of 20 mL glycerol. After stirring for 0.5 h, the homogeneous solution was transferred into a Teflon-lined stainless steel autoclave, which was maintained at 180 °C for 6 h. The formed precipitate was washed with deionized water and ethanol and dried at 60 °C overnight, followed by calcination at 600 °C for 3 h to obtain Mn_2O_3. The mixed-phase manganese oxide (MnO_x) was prepared by a similar procedure, except for the metal precursors are changed to manganese nitrate and cerium nitrate with the molar ratio of 25:1. Mn_3O_4 was obtained in a commercial way and MnO_x-M was prepared through mechanical mixing of Mn_2O_3 and Mn_3O_4 in the identical mass ratio of MnO_x (Mn_2O_3: Mn_3O_4 = 7: 3). The mass ratio was calculated on Jade on the basis of XRD pattern. The quantitative analysis of fitted profile was performed by using reference intensity ratios (RIR) of standard PDF cards, and the area of peak at around 32.9° and 36.1° was used for the calculation of Mn_2O_3 and Mn_3O_4, respectively.

2.2. Catalyst characterization

The structural and physicochemical properties of catalysts were characterized by X-ray diffraction (XRD), Raman spectroscopy, high-resolution transmission electron microscope (HR-TEM), X-ray

absorption near-edge spectra (XANES), extended X-ray absorption fine spectra (EXAFS), X-ray photoelectron spectroscopy (XPS), electron paramagnetic resonance (EPR), hydrogen temperature-programmed reduction (H_2-TPR), oxygen/ammonia/CB temperature-programmed desorption (O_2/NH_3/CB-TPD). In situ TPD and DRIFTS measurements were used for AOS exploration and mechanism study. The details of various characterization procedures are presented in Supporting Information.

2.3. Catalytic performance evaluation

CB oxidation reactions were evaluated in a fixed-bed heterogeneous micro-reactor, and 0.4 g catalyst was employed under the gas mixture of 500 ppm CB and 21% O_2/N_2 (and 3 vol% H_2O when needed), giving a gas hourly space velocity of 22500 mL·g^{-1}·h^{-1}. The concentrations of CB and chlorinated organics were detected by an Agilent 6890 gas chromatograph equipped with a flame ionization detector (FID). Other products (CO, CO_2 and HCl) were analyzed by an on-line FTIR spectrometer (MKS, MultiGas 2030). The conversion of CB and yields of CO_2, CO and HCl were calculated according to following equations:

$$X = \frac{[CB]_{in} - [CB]_{out}}{[CB]_{in}} \times 100\% \tag{1}$$

$$Y_{CO_2} = \frac{[CO_2]_{out}}{6[CB]_{in}} \times 100\% \tag{2}$$

$$Y_{CO} = \frac{[CO]_{out}}{6[CB]_{in}} \times 100\% \tag{3}$$

$$Y_{CO_x} = \frac{[CO_2]_{out} + [CO]_{out}}{6[CB]_{in}} \times 100\% \tag{4}$$

$$Y_{HCl} = \frac{[HCl]_{out}}{[CB]_{in}} \times 100\% \tag{5}$$

where $[CB]_{in}$ and $[CB]_{out}$ denote the concentrations of CB fed into and flowing out of the reactor, and $[CO]_{out}$, $[CO_2]_{out}$ and $[HCl]_{out}$ represent the concentrations of CO, CO_2 and HCl in the outlet gas, respectively.

The details of kinetic measurements are provided in Supporting Information.

3. Results and discussion

3.1. Structural properties

The crystal structure of as-obtained catalysts was analyzed by XRD. The diffraction peaks of Mn_2O_3 and Mn_3O_4 are well indexed to cubic Mn_2O_3 (JCPDS 41-1442) and tetragonal Mn_3O_4 (JCPDS 24-0734), respectively (Fig. 1a). The patterns of MnO_x and MnO_x-M demonstrate their structure of dual-phase Mn_2O_3-Mn_3O_4. Noticeably, the diffraction peak corresponding to Mn_2O_3 (222) plane shifts to a lower value on MnO_x (Fig. 1b), and the lattice constant in MnO_x (9.418 Å) gets larger than Mn_2O_3 and MnO_x-M (9.409 Å), indicating the in situ formed Mn_3O_4-Mn_2O_3 dual phases affect the lattice structure of MnO_x. The crystallite sizes of catalysts are calculated based on Scherer's equation (Table S1), and the interfacial structure decreases the size of MnO_x to some extent. All catalysts possess mesoporous structure (Fig. S1), and the specific surface area (S_{BET}) are summarized in Table S1.

Raman spectroscopy was used to further identify the structure of catalysts (Fig. 1c). The peaks at around 259/281, 312, 367 and 651 cm^{-1} are active modes of Mn_3O_4, where the strong peak at 651 cm^{-1} corresponds to the Mn—O stretching vibration of Mn^{2+} [21, 22]. The bands at 621/642 and 693 cm^{-1} should be attributed to the asymmetric stretching of Mn—O—Mn and symmetric stretching of Mn_2O_3 groups, respectively [23,24]. Compared with Mn_2O_3 and Mn_3O_4,
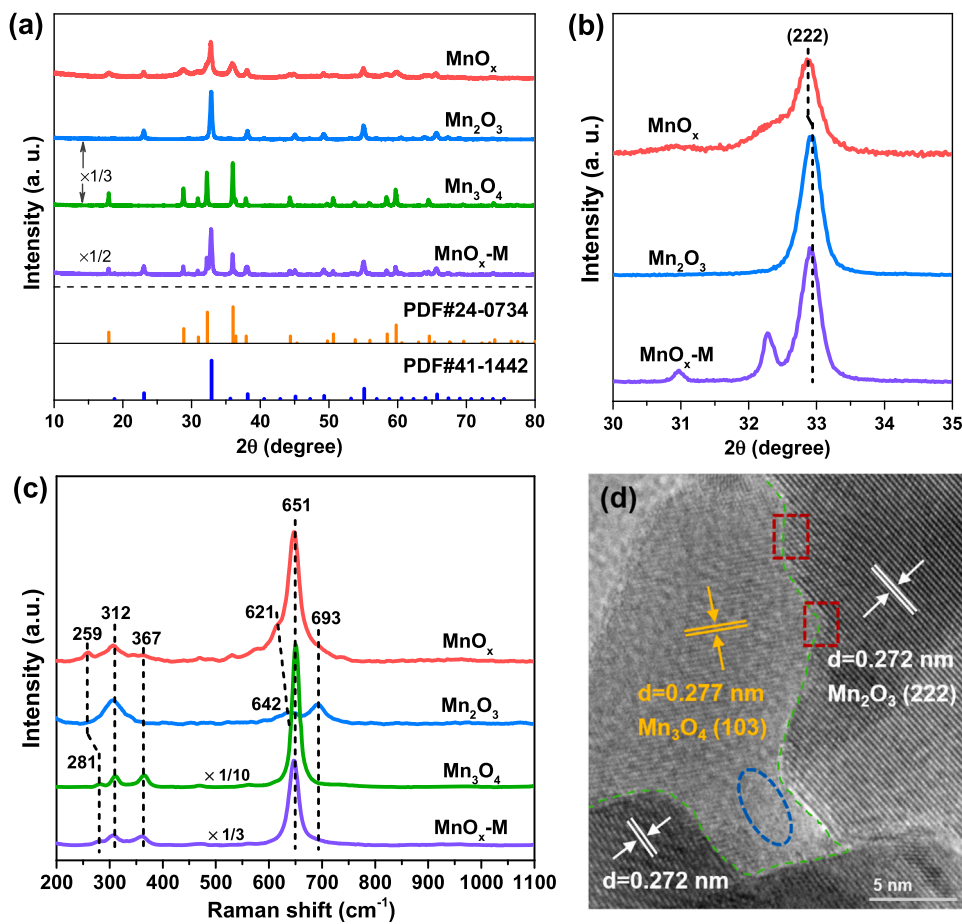
Fig. 1. (a, b) XRD patterns and (c) Raman spectra of as-obtained catalysts, (d) HRTEM image of MnO_x.

the Raman peaks of MnO_x at 259 and 621 cm^{-1} are distinctly red-shifted, implying the weakening of Mn—O bond strength based on Hooke's law [25]. Weaker metal—oxygen strength could promote the formation of oxygen vacancies to activate molecular oxygen, and concurrently boost the mobility of lattice oxygen [26], which are crucial for catalytic oxidation reactions.

HR-TEM images show that Mn_3O_4 exposes (112) plane and Mn_2O_3 presents (211) and (222) planes (Fig. S2a and b). As for MnO_x (Fig. 1d), the *d*-spacing of 0.272 and 0.277 nm are ascribed to Mn_2O_3 (222) plane and Mn_3O_4 (103) plane, respectively. The interface between Mn_2O_3 and Mn_3O_4 can be observed and marked by green bight. Defects (red square) could be found existing on lattice fringes of Mn_2O_3 adjacent to the interface, and the blurry lattice fringes of Mn_3O_4 (blue ellipse) indicate the emergence of vacancies [27]. These structural defects/vacancies, originating from the lattice mismatch/distortion at the dual-phase interface, could stimulate the generation and activity of oxygen species [28]. Simple mechanical mixing fails to bring about intimate interaction, resulting in the separation of two oxides (Fig. S2c and d).

3.2. Chemical states, surface acidity and CB adsorption

Chemical status of as-obtained catalysts was characterized by XPS measurements. Mn $2p_{3/2}$ spectra (Fig. S3a) are deconvoluted into three peaks at around 640.6, 641.7 and 643.2 eV, ascribed to Mn^{2+}, Mn^{3+} and Mn^{4+}, respectively [29,30]. The average valence state (AVS) of Mn that is calculated based on Mn 3 s spectra (Fig. S3b) declines with the increase of Mn_3O_4 content and Mn^{2+} proportion (Table S2). The result of Mn K-edge XANES further proves the Mn oxidation state declines as $Mn_2O_3 > MnO_x > Mn_3O_4$ (Fig. 2c). Three oxygen species are detected in O 1 s spectra (Fig. 2a), that are O_{latt} (surface lattice oxygen) at around

529.7 eV, O_{ads} (surface adsorbed oxygen) at about 531.3 eV and O_{OH} (oxygen in surface adsorbed water) at around 532.9 eV [31,32]. Noteworthily, the binding energies of O_{latt} and O_{ads} on MnO_x are visibly lower than the other catalysts, suggesting the higher electron density of these oxygen species. The increase of electron cloud density has been revealed to be beneficial for boosting the activity of oxygen species [26]. Moreover, larger amount of O_{ads} (30.7%) on MnO_x implies the unique biphase interface facilitates O_{ads} formation (Table S2), hence enhancing the catalytic performance, especially in low-temperature region. O_{ads} is closely associated with oxygen vacancy [33], and the result of EPR reveals the interface also promotes the generation of oxygen vacancy on MnO_x (Fig. 2b). According to the EXAFS analysis (Fig. 2d and Fig. S3d), the Mn—O coordination number of MnO_x is lower than that of Mn_2O_3 and Mn_3O_4 (Table S3), which could be the result of abundant structural defects and in favor of the formation of oxygen vacancy.

Surface acidity could be vital for adsorption/activation of reactant molecules, which was studied by NH_3-TPD (Fig. S4). The overlapped desorption profiles (except for Mn_3O_4) are deconvoluted into two peaks that are assigned to NH_3 physical adsorption (ca. 100 °C) and NH_3 adsorption at weak acid sites (150–250 °C) [34,35]. Mn_3O_4 shows scarce acidity or physical adsorption of NH_3. The acidity of MnO_x is distinctly stronger than other catalysts, which is certified by the higher desorption temperature (190 °C) and larger corresponding peak area. Furthermore, CB-TPD measurements directly confirm the greater capacity of MnO_x for CB adsorption, as the desorption peak over MnO_x appears at much higher temperature (371 °C), with the peak area over 7 times larger than that of Mn_2O_3 (Fig. S5). The stronger surface acidity and superior CB adsorption ability, originating from the formed unique interface, could accelerate the activation/cleavage of C—Cl bond and the following oxidation of CB.
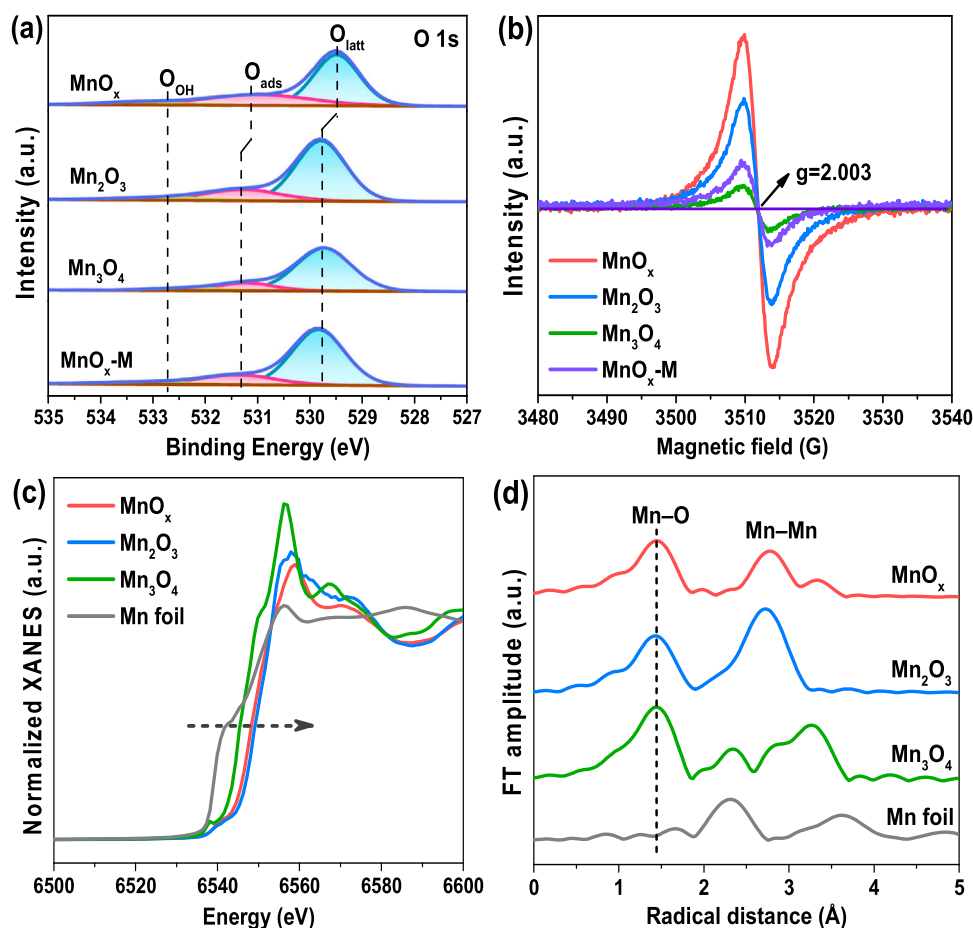
Fig. 2. (a) O 1 s XPS spectra, (b) EPR profiles, (c) Mn K-edge normalized XANES curves and (d) R-space spectra from Mn K-edge EXAFS of catalysts.

3.3. Oxygen species mobility and catalyst reducibility

The mobility of oxygen species was explored by O_2-TPD technique (Fig. 3a). Generally, the desorption peaks at 200–450 °C, 450–700 °C and over 700 °C are assigned to O_{ads}, O_{latt} and $O_{latt-bulk}$ (bulk lattice oxygen), respectively [18,36]. No obvious signals are detected over Mn_3O_4, while Mn_2O_3 and MnO_x-M only have one desorption peak related to $O_{latt-bulk}$, suggesting the oxygen species are stubborn on these catalysts. Notably, besides the $O_{latt-bulk}$, two peaks of O_{ads} and O_{latt} are distinctly observed on MnO_x, which indicates the formed interface and lattice distortion facilitate the formation and mobility of these AOS. As catalytic activities have a positive correlation with the mobility of O_{ads} and O_{latt} [2,37], the unique Mn_2O_3—Mn_3O_4 interface is certified conducive to improving CB oxidation.

H_2-TPR measurements were performed to investigate the influence of interface on catalysts reducibility (Fig. 3b). Mn_3O_4 shows one peak at 422 °C, due to the reduction of Mn_3O_4 to MnO [38]. Two peaks centered at 270 °C and 370 °C on Mn_2O_3 are ascribed to the reduction of Mn_2O_3 to Mn_3O_4 and Mn_3O_4 to MnO, respectively. For MnO_x, the peak appears at much lower temperature (188 °C) could be attributed to the H_2 consumption by oxygens near the Mn_2O_3—Mn_3O_4 interface [39]. The disordered lattice and structural defects alter the electronic structure, weaken the Mn—O strength and improve oxygen mobility, resulting in MnO_x presenting more outstanding reducibility. The profile of MnO_x-M is similar to that of Mn_2O_3 combined with Mn_3O_4, proving the simple mixture of two phases cannot promote the reducibility of original oxides.

3.4. Catalytic performance assessment

Catalytic activities and yields of CO_x (CO_2 and CO) and HCl over obtained catalysts are shown in Fig. 4. According to the conversion curves (Fig. 4a) and T_{50} and T_{90} (temperature for 50 % and 90 % conversion of CB) listed in Table S1, the activity of catalysts follows the order of MnO_x > Mn_2O_3 > MnO_x-M > Mn_3O_4, where MnO_x presents a remarkable advantage in activity as compared to pure Mn_2O_3 and Mn_3O_4. Although the mechanically-mixed MnO_x-M contains the same two phases, its activity is distinctly inferior to MnO_x, with the T_{90} increasing by ca. 30 °C, which manifests the unique interfacial structure in MnO_x (not simple coexistence of two substances) is crucial for the high activity. The comparison of reaction rate also proves the outstanding activity of MnO_x (Fig. S6a), while the results of specific reaction rate suggest that the increase of specific surface area does not affect the catalytic activity prominently (Fig. S6b). Besides, the activity of MnO_x shows an advantage as compared with many previously reported catalysts (Table S4). Based on Arrhenius equation, the apparent activation energy (E_a) of catalysts is calculated (Fig. 4b) and in the sequence of MnO_x (41.7 kJ/mol) < Mn_2O_3 (58.0 kJ/mol) < MnO_x-M (61.7 kJ/mol) < Mn_3O_4 (100.6 kJ/mol), further validating the superior capacity of MnO_x toward CB activation and degradation.

The yields of CO_x during CB oxidation are depicted in Fig. 4c, which increase with temperature rise for all catalysts. The trend of CO_x production is coincident with catalytic activity, and MnO_x possesses a higher CO_x yield during the reaction. Besides, CO_x yield is close to CB conversion (over 99%) on MnO_x when the temperature reaches 340 °C. For the other catalysts, the CO_x yield is lower than CB conversion, on account of the sluggish oxidation of generated intermediates. The different results demonstrate MnO_x owns the better ability of CB
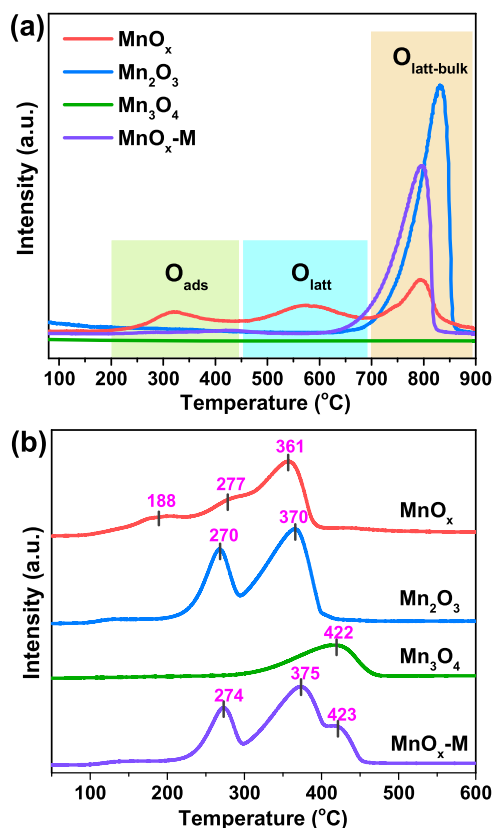
Fig. 3. (a) O_2-TPD and (b) H_2-TPR results of obtained catalysts.

mineralization. Due to continuous CB decomposition, HCl yield over Mn_3O_4 consecutively goes up with temperature increase (Fig. 4d). Benefiting from higher CB conversion efficiency, HCl production is also much higher on MnO_x before 300 °C. The decline afterward results from the oxidation of dissociated Cl/HCl into gaseous Cl_2 via Deacon reaction, which could be accelerated at elevated temperature [40]. This similar phenomenon can be found on Mn_2O_3 and MnO_x-M. The result of HCl yields further proves the high activity of MnO_x for CB destruction, while the lower HCl production at high temperature is due to the superior oxidation ability (more HCl are oxidized into Cl_2).

Several chlorinated byproducts were detected during CB oxidation (Fig. 5), including trichloromethane ($CHCl_3$), tetrachloromethane (CCl_4), trichloroethylene (C_2HCl_3) and perchloroethylene (C_2Cl_4). Except for Mn_3O_4, the byproducts increase first and then reduce with the rise of temperature over the other obtained catalysts. The formed short-chain chlorinated organics stem from the breakage of aromatic ring and chlorination, which could be further oxidized into final inorganic products. The maximum concentrations of byproducts occur at lower temperature over MnO_x, manifesting it is more capable of decomposing CB into intermediates, and the total oxidation of generated byproducts is accomplished at lower temperature. These results evidence that MnO_x has better ability of CB decomposition and deep oxidation of intermediates, in accordance with its outstanding catalytic activity. Due to the inferior reactivity of Mn_3O_4, the formation of byproducts requires higher temperature, and the absence of C_2HCl_3 and C_2Cl_4 possibly means a distinct reaction process.

Additionally, CB conversion over MnO_x is well maintained at about 90% within 30 h (Fig. S7a), revealing its good long-term stability. As water vapor generally exists in varied heterogeneous catalytic oxidation processes, the influence of H_2O is also investigated. The addition of H_2O turns out an increase on CB conversion to some extent, possibly owing to the occurrence of hydrolysis oxidation process, where H_2O molecules are dissociated and react with oxygen species to generate *OOH with higher activity [32]. Moreover, the catalytic activity is also remained on the whole in a cycle test (Fig. S7b), further demonstrating the strong durability of MnO_x.
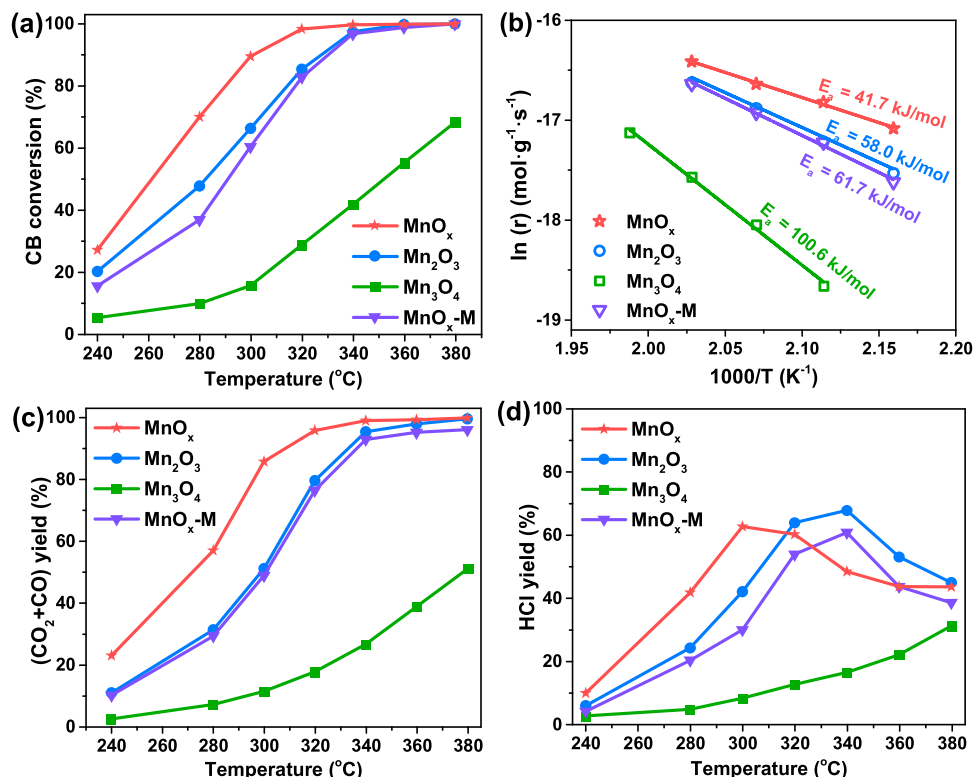

Fig. 4. (a) CB conversion curves, (b) Arrhenius plots, the yield of (c) CO_x and (d) HCl in CB oxidation.
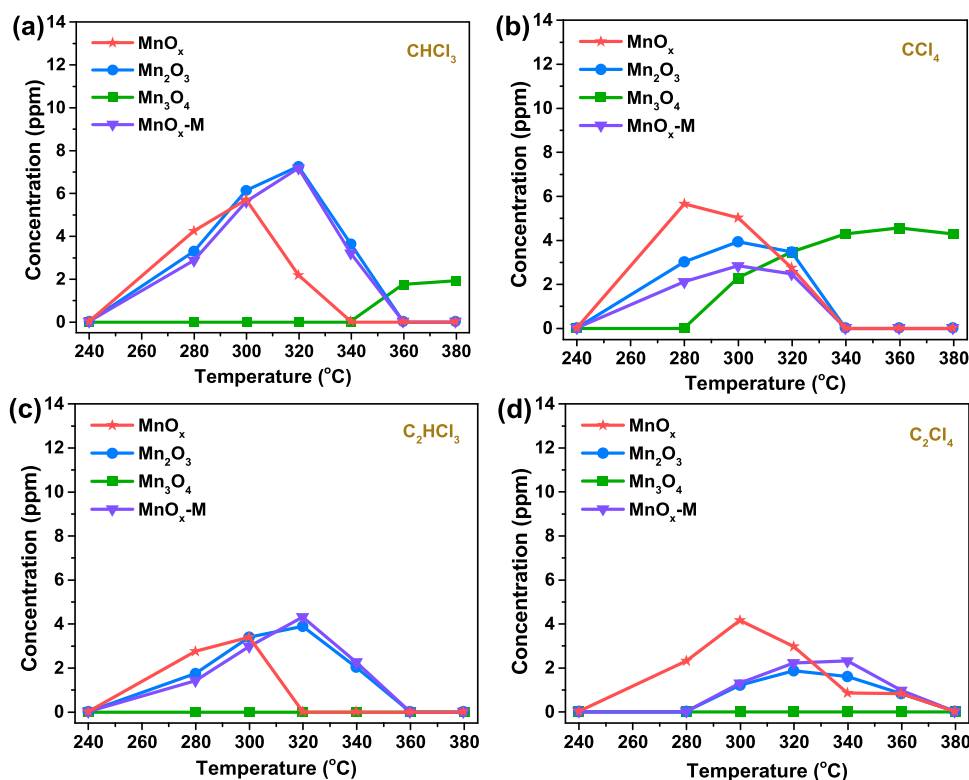
Fig. 5. Distribution of various chlorinated byproducts over as-obtained catalysts during CB oxidation.

3.5. Identification of AOS in CB catalytic oxidation

During CB catalytic oxidation, the evolution of CB conversion as a function of reaction time under stepwise rising temperatures is illustrated in Fig. 6. A gradual decline is observed at relative low temperatures (< 300 °C), yet the CB conversion is stable over 300 °C. Given that VOCs oxidation is a typical oxygen-involved heterogeneous catalytic reaction, this disparity of reaction process under different temperatures suggests the AOS could be inhomogeneous in successive CB oxidation on MnO_x. Accordingly, a series of well-designed in situ TPD experiments combined with isotope-labeled pulse techniques are performed, in order to explore the AOS in CB oxidation under diverse temperature conditions.

Firstly, TPD under helium stream (He-TPD) is conducted to investigate the oxygen consumption by CB oxidation at 240 °C. As blank control, three kinds of oxygen species (O_{ads}, O_{latt} and $O_{latt-bulk}$) are desorbed from pristine MnO_x (Fig. 7a), consistent with its O_2-TPD result.
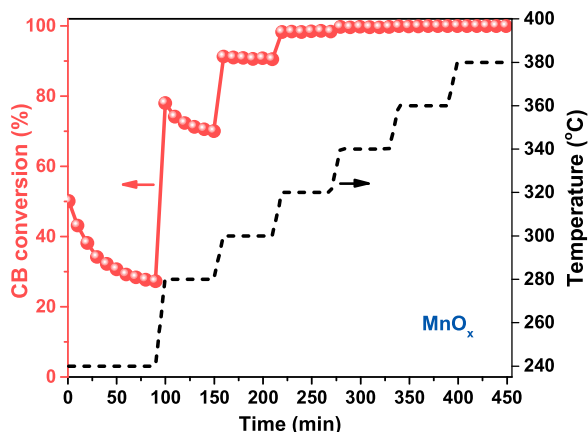

Fig. 6. Time-dependent CB conversion during CB oxidation over MnO_x.

After CB oxidation for 0.5 h, the desorption of O_{ads} vanishes while another two peaks are unaltered, suggesting that only O_{ads} are consumed by CB molecules. The generation of CO_2 confirms the occurrence of CB oxidation at 240 °C (Fig. S8a). Additionally, a CB-pulse experiment with O isotope labeling is designed to further verify the reactivity of O_{ads}. The O_{ads} are first desorbed via He treatment (at 450 °C), followed by oxygen complement under $^{18}O_2$/He stream at 240 °C, thereupon the O atoms of O_{ads} are ^{18}O while that of O_{latt} are original ^{16}O. Fig. 7b and 7e evidence the successful O_{ads} thermal desorption and replenishment (at 240 °C). Afterwards, CB pulse is injected onto catalyst surface to be oxidized, and the signals of $C^{16}O^{16}O/C^{16}O^{18}O/C^{18}O^{18}O$ are recorded (Fig. 7c). The cyclical peaks of $C^{18}O^{18}O$ are clearly detected but inappreciable $C^{16}O^{16}O$ and $C^{16}O^{18}O$ could be observed, which further proves only O_{ads} participate in CB oxidation at 240 °C.

Based on this result, we deduce the decline of activity could be associated with the deterioration of O_{ads} at 240 °C. Therefore, He-TPD is carried out after the catalyst was used for different time at 240 °C under the activity-evaluating condition (Fig. 7d). With the extension of reaction time, the peak area (PA) of desorbed O_{ads} gets smaller and the desorption temperature becomes higher, which means both the amount and activity of O_{ads} decrease with CB oxidation proceeding. Generally, the consumed O_{ads} should be supplemented by gaseous oxygen or lattice oxygen to maintain continuous VOCs oxidation [41]. Thus, O_2-complement experiment followed by He-TPD is employed to deeply study this degeneration of O_{ads}. After the consumption of O_{ads} by CB at 240 °C, 5% O_2/He is introduced for O_{ads} complement and the result of subsequent He-TPD is displayed in Fig. 5e. Although the consumed O_{ads} could be replenished to some extent, the PA of supplemented O_{ads} (denoted as O_{ads}-R) decreases to less than 1/3 of original O_{ads}. More importantly, the O_{ads}-R desorption temperature gets distinctly higher, which indicates the mobility and activity of supplemented O_{ads}-R are inferior to that of pristine catalyst, in accordance with the decline of CB conversion. Further, a successive experiment of O_2 (thermal) desorption → O_2 complement → He-TPD is executed. Through the O_2-complement procedure at 240 °C, O_{ads} have also been supplemented and denoted as
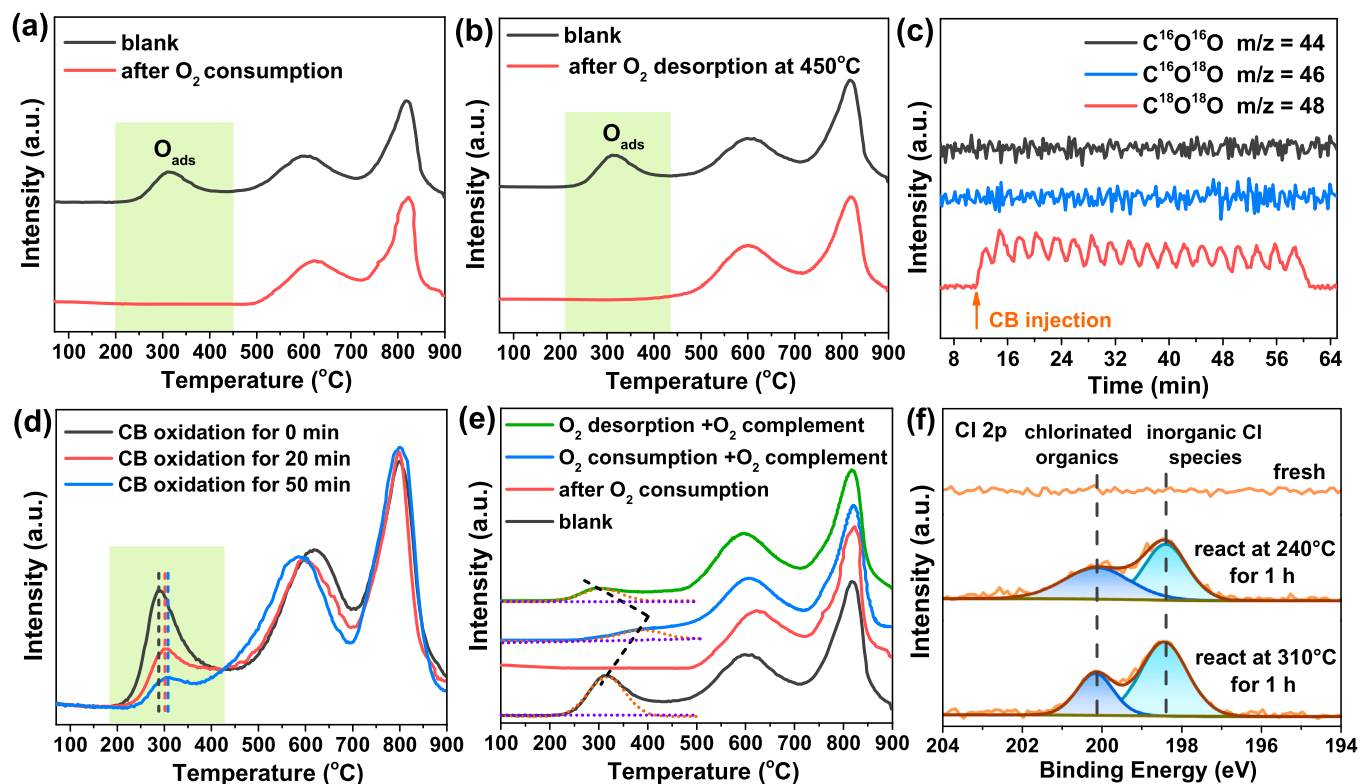
Fig. 7. (a, b) He-TPD profiles of pristine MnO$_x$ and MnO$_x$ pretreated by O$_2$ consumption and O$_2$ desorption, (c) signals of CO$_2$ in CB-pulse experiment at 240 °C, (d) He-TPD profiles of MnO$_x$ used for CB oxidation at 240 °C for different time, (e) He-TPD profiles after distinct treatment procedures, (f) Cl 2p XPS spectra of MnO$_x$ after reaction.
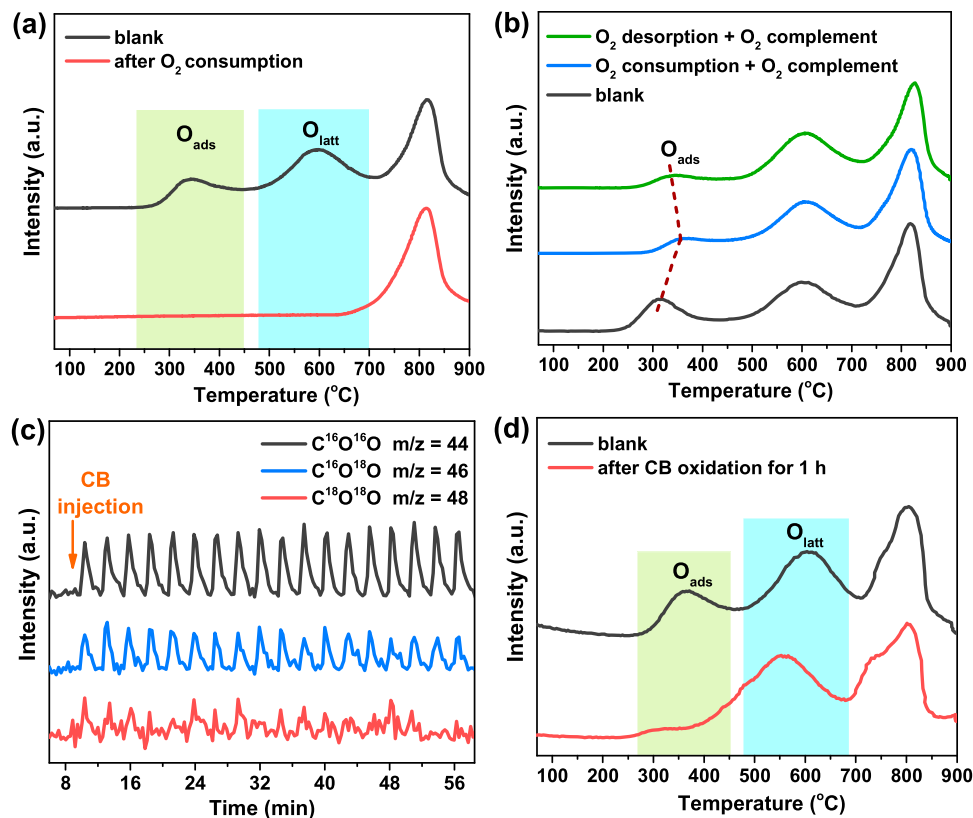

Fig. 8. (a) He-TPD profiles of MnO$_x$ pretreated by O$_2$ consumption at 310 °C, (b) He-TPD profiles after different treatment procedures, (c) signals of CO$_2$ in CB-pulse experiment at 310 °C and (d) He-TPD profiles of MnO$_x$ after CB oxidation at 310 °C for 1 h.

O_{ads}-D. Notably, the desorption temperature of O_{ads}-D is much lower than O_{ads}-R, along with PA of O_{ads}-D larger than O_{ads}-R (Fig. 7e and S8b), signifying the mobility and activity of O_{ads}-D are higher than that of O_{ads}-R. In view of above results, it can be concluded that O_{ads} are AOS for CB oxidation over MnO_x at relatively low temperature (240 °C). Meanwhile, the continuous decline of CB conversion is due to that the consumed O_{ads} (by CB) can only be partially complemented, and the supplemented O_{ads} lose their initial activity for reaction. This negative effect should be related to surface accumulation of chlorine. The dissociated Cl from CB decomposition would be captured in oxygen vacancies [42], occupying the gaseous oxygen-activation sites, hindering the complement of O_{ads} and impairing the activity of supplemented O_{ads}. The Cl 2p XPS spectra (Fig. 7f) provide the support of surface Cl accumulation on used MnO_x.

In order to probe the AOS at high temperatures, the experiment of CB oxidation (at 310 °C) → He-TPD is accomplished (Fig. 8a). The disappearance of desorption peaks that belong to O_{ads} and O_{latt} clarifies these two oxygen species could both react with CB at 310 °C, which is confirmed by CO_2 production (Fig. S8c). Considering that the catalyst activity is stable at high temperatures, two inferences are made under this condition: (i) the consumed O_{ads} could be effectively supplemented without activity loss when temperature is elevated, (ii) O_{latt} play the leading role in sustaining the CB conversion at high temperatures. To explore the former deduction, O_2 complements at 310 °C are performed after O_{ads} consumption by CB and thermal desorption, respectively, accompanied with the subsequent He-TPD (Fig. 8b). The replenished O_{ads} after CB oxidation (denoted as O_{ads}-RH) still show a lower activity/ mobility than blank control and O_{ads}-DH (the supplemented O_{ads} after O_2 desorption with He), which means the activity of O_{ads}-RH cannot restore to the original level even if temperature rises up. This manifests O_{ads} are not primary AOS for CB oxidation at high temperature, and the steady activity should be closely associated with O_{latt}. Consequently, the CB-pulse experiment with O isotope labeling is also used for scrutinizing

the function and property of O_{latt}. The peaks of three carbon dioxide appear synchronously, but the intensity of $C^{16}O^{16}O$ is remarkably higher than $C^{18}O^{18}O$ (Fig. 8c), hinting that O_{ads} and O_{latt} could both participate in CB oxidation while O_{latt} are predominant AOS that participate in CB oxidation. The detection of $C^{16}O^{18}O$ could be due to the oxygen exchange between gaseous $^{18}O_2$ and partial O_{latt} (^{16}O) [43]. In addition, O_{ads} signal diminishes significantly after the pristine catalyst is used for 1 h at 310 °C under activity-evaluating condition (Fig. 8d). Conversely, the content of O_{latt} is well remained, demonstrating the consumed O_{latt} can be effectively supplemented by gaseous oxygen during the reaction. Interestingly, the desorption peaks of O_{ads} and O_{latt} both shift to lower temperature after CB oxidation, which is unexpected and worthy of future study. The surface Cl deposition also happens after the reaction at 310 °C (Fig. 7f), owing to the Cl capture at O_{ads}-activating sites. The surface Cl contents are close after reaction at 240 °C (1.48%) and 310 °C (1.61%), indicating that Cl scarcely occupy the sites of O_{latt} at high temperature. To sum up, O_{latt} can be activated to involve in CB oxidation at high temperature and act as the predominant AOS, which are adequately supplemented and maintain the reactivity in continuous reaction.

3.6. Proposed reaction mechanism

In situ DRIFTS measurements were carried out to unveil the process of CB adsorption and oxidation. When MnO_x is exposed to CB at 240 °C, the bands at 1589 and 1546 cm^{-1} are assigned to phenolate vibration and stretching vibration of benzoquinone [15,44,45], respectively (Fig. 9a), which indicate the oxidation of adsorbed CB. The peaks at 1523 and 1307 cm^{-1} correspond to surface maleate species [46,47], while the band at 1492 cm^{-1} represents in-plane vibration of aromatic ring [15]. Additionally, the band located at 1444 cm^{-1} is related to acetate [45], and another strong peak at 1403 cm^{-1} is ascribed to —CH bending of formate species [48]. The formation of these intermediates
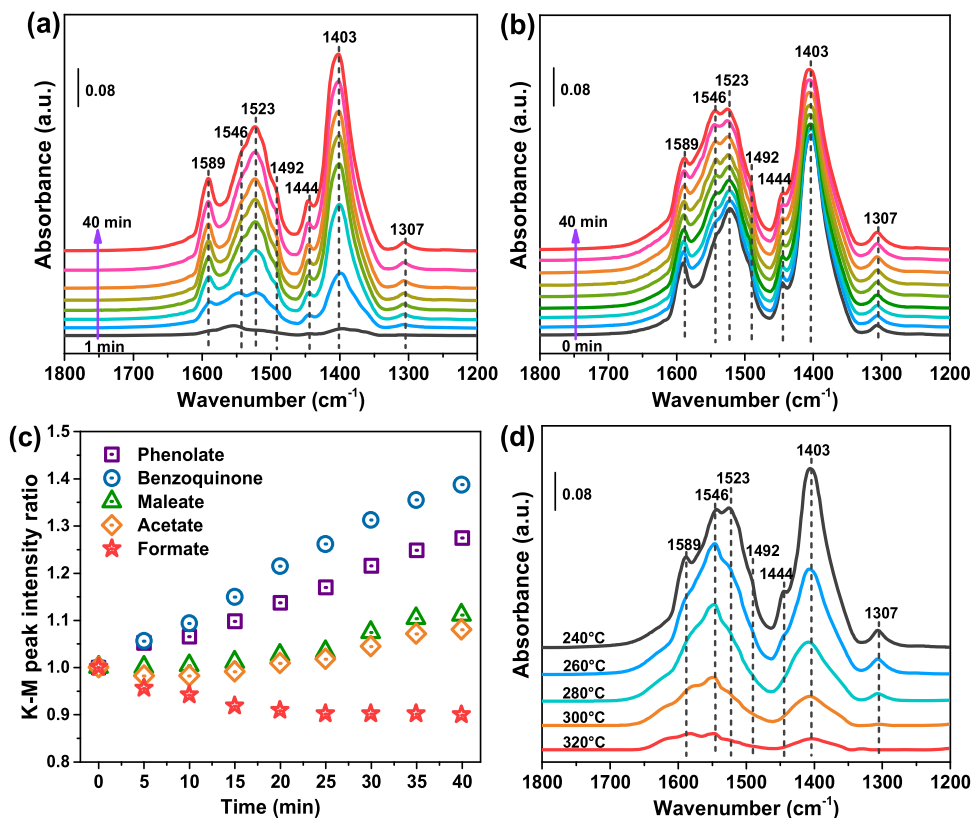

Fig. 9. In situ DRIFTS spectra of (a) CB adsorption and (b) CB oxidation on MnO_x at 240 °C, (c) variation of peak intensity during CB oxidation, (d) in situ DRIFTS spectra of CB oxidation at various temperatures.

demonstrates the reaction of adsorbed CB with O_{ads} of MnO_x, and due to the surface accumulation, the intensity of these bands gets stronger with time extension. Besides the aforementioned intermediates, chlorinated acetate (1565 cm^{-1}) and bidentate formate (1337 cm^{-1}) are observed on MnO_x-M (Fig. S9a) [47,49]. In comparison, the higher peaks intensity on MnO_x proves its better capacity for CB adsorption and decomposition.

Upon introducing O_2 into feed gas at 240 °C, the species of intermediates remain unchanged on MnO_x, with the variations of bands intensity are observed distinctly (Fig. 9b). The ratios of peaks intensity are calculated, taking the spectrum after CB adsorption for 40 min as a basis, and displayed in Fig. 9c. Except for formate, the other intermediates (phenolate, benzoquinone, acetate and maleate) constantly accumulate on surface due to the continuous CB oxidation. The decrease of formate manifests the C_1 organic molecule is easier to be converted. According to DRIFTS results and previous reports [32,50], CB oxidation over MnO_x could proceed via the pathway of CB → phenolate → benzoquinone → maleate → acetate and formate → final products (Fig. S10), where maleate comes from the cracking of benzoquinone. The accumulation rate of benzoquinone is the highest while that of maleate and acetate are much lower (Fig. 9c), signifying the benzoquinone transformation is more difficult than other intermediates, that is, the cleavage of aromatic ring could be the rate-determining step for CB oxidation. The time-dependent spectra of MnO_x-M (Fig. S9b and c) show that all intermediates continuously accumulate on catalyst surface, and the increase of formate further reveals the lower activity of the mechanically mixed catalyst. Moreover, remarkable accumulation of chlorinated acetate is found, evidencing that this Cl-containing species is also difficult to be oxidized.

Due to deeper oxidation of CB, raising reaction temperature leads to the reduction of peak intensity of various intermediates (Fig. 9d). The decline of formate is the fastest (Fig. S11), further verifying its facile conversion on MnO_x. Meanwhile, because of arduous breakage of aromatic ring, the decomposition of benzoquinone and phenolate need higher temperature. For MnO_x-M catalyst, the evolution trends of most intermediates are similar to MnO_x (Fig. S12). Notably, the chlorinated acetate increases when temperature rises from 240 °C to 260 °C, and its subsequent degradation rate is also distinctly lower than maleate, acetate and formate. Therefore, besides aromatic ring cleavage, the torpid decomposition of chlorinated acetate could be another factor that limits the CB oxidation on MnO_x-M and causes its inferior activity.

Interestingly, the abovementioned analyses of O_{ads} and O_{latt} are also supported by in situ DRIFTS. Both pristine and pre-treated MnO_x (the treatment is thermal desorption of O_{ads} under He stream at 450 °C) are used for adsorbing CB at 240 °C and 310 °C, and the DRIFTS spectra are recorded (Fig. S13). After pretreatment, the peak intensity of surface intermediates dramatically decrease at 240 °C, whereas only a slight decline is observed at 310 °C as compared with pristine MnO_x. This difference further suggests O_{ads} participate in CB oxidation at 240 °C, the effect of which gets negligible at high temperature.

4. Conclusions

In summary, the generation and reactivity of AOS (O_{ads} and O_{latt}) are boosted by constructing dual-phase MnO_x with novel Mn_2O_3—Mn_3O_4 interface. The abundant interface induces lattice distortion, which facilitates the formation of oxygen vacancy and O_{ads}, and enhances the mobility of O_{latt}. The catalyst reducibility and adsorption capacity towards reactant are also augmented thanks to the interfacial structure. Consequently, MnO_x exhibits distinctly higher activity with excellent stability in CB deep oxidation. Based on in situ TPD techniques, O_{ads} function as AOS at relatively low temperature (240 °C), which cannot be entirely replenished due to Cl occupation at oxygen vacancies. At higher temperature (310 °C), AOS switch to O_{latt} that could be effectively supplemented and maintain its original reactivity. Furthermore, in situ DRIFTS results reveal that CB oxidation over MnO_x follows the pathway

of CB → phenolate → benzoquinone → maleate → acetate and formate → inorganic products, where the cleavage of aromatic ring is the rate-determining step. This study affords in-depth insight into the promotion and dynamic evolution of AOS in heterogeneous catalytic oxidation processes, which could also provide the guidance for developing desirable catalysts for environmental catalysis.

CRediT authorship contribution statement

Xiaoxiao Duan: Investigation, Formal analysis, Validation, Writing – original draft, Writing – review & editing. **Ting Zhao:** Methodology, Validation, Formal analysis. **Zhenwen Yang:** Formal analysis, Writing – review & editing. **Ben Niu:** Data curation, Formal analysis. **Ganggang Li:** Methodology, Formal analysis. **Bingzhi Li:** Formal analysis, Data curation, Writing – review & editing. **Zhongshen Zhang:** Validation, Writing – review & editing, Funding acquisition. **Jie Cheng:** Validation, Writing – review & editing. **Zhengping Hao:** Formal analysis, Writing – review & editing, Supervision, Funding acquisition.

Declaration of Competing Interest

The authors declare that they have no known competing financial interests or personal relationships that could have appeared to influence the work reported in this paper.

Data availability

Data will be made available on request.

Appendix A. Supporting information

Supplementary data associated with this article can be found in the online version at doi:10.1016/j.apcatb.2023.122719.

References

[1] Q. Fu, W.-X. Li, Y. Yao, H. Liu, H.-Y. Su, D. Ma, X.-K. Gu, L. Chen, Z. Wang, H. Zhang, B. Wang, X. Bao, Interface-confined ferrous centers for catalytic oxidation, Science 328 (2010) 1141–1144.

[2] Y. Fang, Q. Zhang, H. Zhang, X. Li, W. Chen, J. Xu, H. Shen, J. Yang, C. Pan, Y. Zhu, J. Wang, Z. Luo, L. Wang, X. Bai, F. Song, L. Zhang, Y. Guo, Dual activation of molecular oxygen and surface lattice oxygen in single atom Cu_1/TiO_2 catalyst for CO oxidation, Angew. Chem. Int. Ed. 61 (2022), e202212273.

[3] Y. Yang, H. Fei, G. Ruan, J.M. Tour, Porous cobalt-based thin film as a bifunctional catalyst for hydrogen generation and oxygen generation, Adv. Mater. 27 (2015) 3175–3180.

[4] F. You, J. Wan, J. Qi, D. Mao, N. Yang, Q. Zhang, L. Gu, D. Wang, Lattice distortion in hollow multi-shelled structures for efficient visible-light CO_2 reduction with a SnS_2/SnO_2 junction, Angew. Chem. Int. Ed. 59 (2020) 721–724.

[5] B.H.R. Suryanto, Y. Wang, R.K. Hocking, W. Adamson, C. Zhao, Overall electrochemical splitting of water at the heterogeneous interface of nickel and iron oxide, Nat. Commun. 10 (2019) 5599–5609.

[6] M.A. Ahsan, A.R. Puente Santiago, Y. Hong, N. Zhang, M. Cano, E. Rodriguez-Castellon, L. Echegoyen, S.T. Sreenivasan, J.C. Noveron, Tuning of trifunctional NiCu bimetallic nanoparticles confined in a porous carbon network with surface composition and local structural distortions for the electrocatalytic oxygen reduction, oxygen and hydrogen evolution reactions, J. Am. Chem. Soc. 142 (2020) 14688–14701.

[7] A. Ruiz Puigdollers, P. Schlexer, S. Tosoni, G. Pacchioni, Increasing oxide reducibility: the role of metal/oxide interfaces in the formation of oxygen vacancies, ACS Catal. 7 (2017) 6493–6513.

[8] J. Saavedra, H.A. Doan, C.J. Pursell, L.C. Grabow, B.D. Chandler, The critical role of water at the gold-titania interface in catalytic CO oxidation, Science 345 (2014) 1599–1602.

[9] G. Chen, Y. Zhao, G. Fu, P.N. Duchesne, L. Gu, Y. Zheng, X. Weng, M. Chen, P. Zhang, C.-W. Pao, J.-F. Lee, N. Zheng, Interfacial effects in iron-nickel hydroxide–platinum nanoparticles enhance catalytic oxidation, Science 344 (2014) 495–499.

[10] M. Guo, P. Ma, J. Wang, H. Xu, K. Zheng, D. Cheng, Y. Liu, G. Guo, H. Dai, E. Duan, J. Deng, Synergy in Au-CuO janus structure for catalytic isopropanol oxidative dehydrogenation to acetone, Angew. Chem. Int. Ed. 61 (2022), e202203827.

[11] B. Ding, P. Zheng, P. Ma, J. Lin, Manganese oxide nanomaterials: synthesis, properties, and theranostic applications, Adv. Mater. 32 (2020) 1905823–1905858.

[12] Y. Yang, S. Zhao, F. Bi, J. Chen, Y. Li, L. Cui, J. Xu, X. Zhang, Oxygen-vacancy-induced O2 activation and electron-hole migration enhance photothermal catalytic toluene oxidation, Cell Rep. Phys. Sci. 3 (2022) 101011–101030.

[13] M. Zhao, J. Deng, J. Liu, Y. Li, J. Liu, Z. Duan, J. Xiong, Z. Zhao, Y. Wei, W. Song, Y. Sun, Roles of surface-active oxygen species on 3DOM cobalt-based spinel catalysts MxCO3–xO4 (M = Zn and Ni) for NOx-assisted soot oxidation, ACS Catal. 9 (2019) 7548–7567.

[14] L. Nie, D. Mei, H. Xiong, B. Peng, Z. Ren, X.I.P. Hernandez, A. DeLaRiva, M. Wang, M.H. Engelhard, L. Kovarik, A.K. Datye, Y. Wang, Activation of surface lattice oxygen in single-atom Pt/CeO2 for low-temperature CO oxidation, Science 358 (2017) 1419–1423.

[15] C. Dong, Z. Qu, Y. Qin, Q. Fu, H. Sun, X. Duan, Revealing the highly catalytic performance of spinel CoMn2O4 for toluene oxidation: involvement and replenishment of oxygen species using in situ designed-TP techniques, ACS Catal. 9 (2019) 6698–6710.

[16] Z. Jiang, M. Tian, M. Jing, S. Chai, Y. Jian, C. Chen, M. Douthwaite, L. Zheng, M. Ma, W. Song, J. Liu, J. Yu, C. He, Modulating the electronic metal-support interactions in single-atom Pt1-CuO catalyst for boosting acetone oxidation, Angew. Chem. Int. Ed. 61 (2022), e202200763.

[17] L. Zhang, W. Deng, Y. Cai, Q. Dai, L. Guo, Comparative studies of phosphate-modified CeO2 and Al2O3 for mechanistic understanding of dichloromethane oxidation and chloromethane formation, ACS Catal. 10 (2020) 13109–13124.

[18] M. Tian, Z. Jiang, C. Chen, M. Kosari, X. Li, Y. Jian, Y. Huang, J. Zhang, L. Li, J.-W. Shi, Y. Zhao, C. He, Engineering Ru/MnCo3Ox for 1,2-dichloroethane benign destruction by strengthening C–Cl cleavage and chlorine desorption: decisive role of H2O and reaction mechanism, ACS Catal. 12 (2022) 8776–8792.

[19] Y.G. Wang, D.C. Cantu, M.S. Lee, J. Li, V.A. Glezakou, R. Rousseau, CO oxidation on Au/TiO2: condition-dependent active sites and mechanistic pathways, J. Am. Chem. Soc. 138 (2016) 10467–10476.

[20] Q. Wang, Y. Li, A. Serrano-Lotina, W. Han, R. Portela, R. Wang, M.A. Banares, K. L. Yeung, Operando investigation of toluene oxidation over 1d Pt@CeO2 derived from Pt cluster-containing MOF, J. Am. Chem. Soc. 143 (2021) 196–205.

[21] Z.-Y. Tian, P. Mountapmbeme Kouotou, N. Bahlawane, P.H. Tchoua Ngamou, Synthesis of the catalytically active Mn3O4 spinel and its thermal properties, J. Phys. Chem. C 117 (2013) 6218–6224.

[22] X. Wu, L. Xia, Y. Wang, W. Lu, Q. Liu, X. Shi, X. Sun, Mn3 o4 nanocube: an efficient electrocatalyst toward artificial N2 fixation to NH3, Small 14 (2018) 1803111–1803117.

[23] J. Xu, Y.-Q. Deng, Y. Luo, W. Mao, X.-J. Yang, Y.-F. Han, Operando raman spectroscopy and kinetic study of low-temperature CO oxidation on an α-Mn2O3 nanocatalyst, J. Catal. 300 (2013) 225–234.

[24] Y.-F. Han, K. Ramesh, L. Chen, E. Widjaja, S. Chilukoti, F. Chen, Observation of the reversible phase-transformation of α-Mn2O3 nanocrystals during the catalytic combustion of methane by in situ raman spectroscopy, J. Phys. Chem. C 111 (2007) 2830–2833.

[25] S. Rong, P. Zhang, F. Liu, Y. Yang, Engineering crystal facet of α-MnO2 nanowire for highly efficient catalytic oxidation of carcinogenic airborne formaldehyde, ACS Catal. 8 (2018) 3435–3446.

[26] Y. Shen, J. Deng, S. Impeng, S. Li, T. Yan, J. Zhang, L. Shi, D. Zhang, Boosting toluene combustion by engineering Co–O strength in cobalt oxide catalysts, Environ. Sci. Technol. 54 (2020) 10342–10350.

[27] N. Huang, Z. Qu, C. Dong, Y. Qin, X. Duan, Superior performance of α@β-MnO2 for the toluene oxidation: active interface and oxygen vacancy, Appl. Catal. A Gen. 560 (2018) 195–205.

[28] R.B. Wexler, G.S. Gautam, E.B. Stechel, E.A. Carter, Factors governing oxygen vacancy formation in oxide perovskites, J. Am. Chem. Soc. 143 (2021) 13212–13227.

[29] Z. Chen, Q. Yang, H. Li, X. Li, L. Wang, S. Chi Tsang, Cr–MnOx mixed-oxide catalysts for selective catalytic reduction of NOx with NH3 at low temperature, J. Catal. 276 (2010) 56–65.

[30] F. Ji, Y. Men, J. Wang, Y. Sun, Z. Wang, B. Zhao, X. Tao, G. Xu, Promoting diesel soot combustion efficiency by tailoring the shapes and crystal facets of nanoscale Mn3O4, Appl. Catal. B Environ. 242 (2019) 227–237.

[31] X. Feng, D. Liu, B. Yan, M. Shao, Z. Hao, G. Yuan, H. Yu, Y. Zhang, Highly active PdO/Mn3O4/CeO2 nanocomposites supported on one dimensional halloysite nanotubes for photoassisted thermal catalytic methane combustion, Angew. Chem. Int. Ed. 60 (2021) 18552–18556.

[32] X. Duan, T. Zhao, B. Niu, Z. Wei, G. Li, Z. Zhang, J. Cheng, Z. Hao, Simultaneously constructing active sites and regulating Mn-O strength of Ru-substituted perovskite for efficient oxidation and hydrolysis oxidation of chlorobenzene, Adv. Sci. 10 (2023), e2205054.

[33] Y. Liu, Y. Peng, M. Naschitzki, S. Gewinner, W. Schollkopf, H. Kuhlenbeck, R. Pentcheva, B. Roldan Cuenya, Surface oxygen vacancies on reduced Co3O4 (100): superoxide formation and ultra-low-temperature CO oxidation, Angew. Chem. Int. Ed. 60 (2021) 16514–16520.

[34] F. Gao, Y. Wang, N.M. Washton, M. Kollár, J. Szanyi, C.H.F. Peden, Effects of alkali and alkaline earth cocations on the activity and hydrothermal stability of Cu/SSZ-13 NH3–SCR catalysts, ACS Catal. 5 (2015) 6780–6791.

[35] F. Wang, J. Ma, G. He, M. Chen, C. Zhang, H. He, Nanosize effect of Al2O3 in Ag/Al2O3 catalyst for the selective catalytic oxidation of ammonia, ACS Catal. 8 (2018) 2670–2682.

[36] G. Shen, R. Zhang, L. Pan, F. Hou, Y. Zhao, Z. Shen, W. Mi, C. Shi, Q. Wang, X. Zhang, J.J. Zou, Regulating the spin state of Fe(III) by atomically anchoring on ultrathin titanium dioxide for efficient oxygen evolution electrocatalysis, Angew. Chem. Int. Ed. 59 (2020) 2313–2317.

[37] J. Yang, S. Hu, Y. Fang, S. Hoang, L. Li, W. Yang, Z. Liang, J. Wu, J. Hu, W. Xiao, C. Pan, Z. Luo, J. Ding, L. Zhang, Y. Guo, Oxygen vacancy promoted O2 activation over perovskite oxide for low-temperature CO oxidation, ACS Catal. 9 (2019) 9751–9763.

[38] H. Pan, Y. Jian, C. Chen, C. He, Z. Hao, Z. Shen, H. Liu, Sphere-shaped Mn3O4 catalyst with remarkable low-temperature activity for methyl-ethyl-ketone combustion, Environ. Sci. Technol. 51 (2017) 6288–6297.

[39] W. Yang, Y. Peng, Y. Wang, Y. Wang, H. Liu, Za Su, W. Yang, J. Chen, W. Si, J. Li, Controllable redox-induced in-situ growth of MnO2 over Mn2O3 for toluene oxidation: active heterostructure interfaces, Appl. Catal. B Environ. 278 (2020) 119279–119290.

[40] N. Li, J. Cheng, X. Xing, Y. Sun, Z. Hao, Distribution and formation mechanisms of polychlorinated organic by-products upon the catalytic oxidation of 1,2-dichloro-benzene with palladium-loaded catalysts, J. Hazard. Mater. 393 (2020) 122412–122421.

[41] Z. Hu, X. Liu, D. Meng, Y. Guo, Y. Guo, G. Lu, Effect of ceria crystal plane on the physicochemical and catalytic properties of Pd/ceria for CO and propane oxidation, ACS Catal. 6 (2016) 2265–2279.

[42] X. Weng, Q. Meng, J. Liu, W. Jiang, S. Pattisson, Z. Wu, Catalytic oxidation of chlorinated organics over lanthanide perovskites: effects of phosphoric acid etching and water vapor on chlorine desorption behavior, Environ. Sci. Technol. 53 (2019) 884–893.

[43] F. Zasada, W. Piskorz, J. Janas, J. Gryboś, P. Indyka, Z. Sojka, Reactive oxygen species on the (100) facet of cobalt spinel nanocatalyst and their relevance in 16O2/18O2 isotopic exchange, deN2O, and deCH4 processes–a theoretical and experimental account, ACS Catal. 5 (2015) 6879–6892.

[44] S.L. Alderman, G.R. Farquar, E.D. Poliakoff, B. Dellinger, An infrared and X-ray spectroscopic study of the reactions of 2-chlorophenol, 1,2-dichlorobenzene, and chlorobenzene with model CuO/silica fly ash surfaces, Environ. Sci. Technol. 39 (2005) 7396–7401.

[45] Y. Sun, S. Xu, B. Bai, L. Li, Y. Kang, X. Hu, Z. Liao, C. He, Biotemplate fabrication of hollow tubular CexSr1–xTiO3 with regulable surface acidity and oxygen mobility for efficient destruction of chlorobenzene: Intrinsic synergy effect and reaction mechanism, Environ. Sci. Technol. 56 (2022) 5796–5807.

[46] H. Huang, Y. Gu, J. Zhao, X. Wang, Catalytic combustion of chlorobenzene over VO/CeO2 catalysts, J. Catal. 326 (2015) 54–68.

[47] L. Li, J.-W. Shi, M. Tian, C. Chen, B. Wang, M. Ma, C. He, In situ fabrication of robust three dimensional ordered macroporous gamma- MnO2/LaMnO3.15 catalyst for chlorobenzene efficient destruction, Appl. Catal. B Environ. 282 (2021) 119565–119577.

[48] N. Li, X. Xing, J. Cheng, Z. Zhang, Z. Hao, Influence of oxygen and water content on the formation of polychlorinated organic by-products from catalytic degradation of 1,2-dichlorobenzene over a Pd/ZSM-5 catalyst, J. Hazard. Mater. 403 (2021) 123952–123962.

[49] P. Sun, S. Zhai, J. Chen, J. Yuan, Z. Wu, X. Weng, Development of a multi-active center catalyst in mediating the catalytic destruction of chloroaromatic pollutants: a combined experimental and theoretical study, Appl. Catal. B Environ. 272 (2020), 119015.

[50] G. Chen, Y. Cai, H. Zhang, D. Hong, S. Shao, C. Tu, Y. Chen, F. Wang, B. Chen, Y. Bai, X. Wang, Q. Dai, Pt and Mo Co-decorated MnO2 nanorods with superior resistance to H2O, sintering, and HCl for catalytic oxidation of chlorobenzene, Environ. Sci. Technol. 55 (2021) 14204–14214.